Journal of Structural Geology 110 (2018) 102–115

Contents lists available at ScienceDirect

Journal of Structural Geology

journal homepage: www.elsevier.com/locate/jsg

Seismically-triggered soft-sediment deformation structures close to a major strike-slip fault system in the Eastern Alps (Hirlatz cave, Austria)

Martina Lan Salomon[a,b], Bernhard Grasemann[a,*], Lukas Plan[c], Susanne Gier[a], Martin P.J. Schöpfer[a]

[a] University of Vienna, Department for Geodynamics and Sedimentology, A-1090 Vienna, Austria
[b] NTNU, Department of Civil and Environmental Engineering, NO-7491 Trondheim, Norway
[c] Natural History Museum Vienna, Karst and Cave Group, A-1010 Vienna, Austria

ARTICLE INFO

Keywords:
Soft-sediment deformation
Liquefaction
Active tectonics
Northern Calcareous Alps
Speleoseismology

ABSTRACT

We investigate episodic soft-sediment deformation structures cross-cut by normal faults preserved in unlithified finely laminated calcite rich sediments in the Hirlatz cave in the Northern Calcareous Alps (Austria). These sediments comprise varve-like alternations of brighter carbonate/quartz rich layers, and darker clay mineral rich layers. The deformed sediments contain abundant millimeter to centimeter-scale soft-sediment structures (load casts, ball-and-pillow structures), sheet slumps (thrust faults and folds), erosive channels filled with slides and chaotic slumps. After deposition and soft-sediment deformation normal faults developed within the entire sedimentary succession, an event that probably correlates with an offset of c. 10 cm of the passage wall above the outcrop. Our major conclusions are: (i) The sediments have a glacial origin and were deposited in the Hirlatz cave under phreatic fluvio-lacustrine conditions. The deposition and the soft-sediment deformation occurred most likely during the last glaciation (i.e. around 25 ka ago); (ii) The liquefaction and formation of the soft-sediment structures in water-saturated stratified layers was triggered by episodic seismic events; (iii) The internally deformed sediments were later displaced by normal faults; (iv) A possible source for the seismic events is the active sinistral Salzach-Ennstal-Mariazeller-Puchberger (SEMP) strike-slip fault which is located about 10 km south of the outcrop and plays a major role in accommodating the extrusion of the Eastern Alps towards the Pannonian Basin. To our knowledge, the described structures are the first report of liquefaction and seismically induced soft-sediment deformations in Quaternary sediments in the Eastern Alps.

1. Introduction

In the Eastern Alps (Austria) and its Neogene basins only few direct geological or geo-archeological evidences are preserved that proof active tectonic processes (e.g. Decker et al., 2005, 2006; Beidinger and Decker, 2011; Beidinger et al., 2011). Although active crustal deformation in the Eastern Alps has been confirmed by numerous geophysical data sets (Reinecker and Lenhardt, 1999; Grenerczy et al., 2005; Tesauro et al., 2006; Brückl et al., 2010; Serpelloni et al., 2016), many geomorphological signals of active crustal deformation have been obliterated by (peri)glacial activity and intensive erosion during the last glacial period (Robl et al., 2008). Karst caves represent a unique environment that is capable to preserve proofs of past geomorphological and geological processes, even in terrains of high surface erosion rates. Especially for paleoseismic and neotectonic studies, this underground archive can play an essential role in deciphering past events (e.g., Postpischl et al., 1991; Lacave et al., 2004; Becker et al., 2006, 2012). Plan et al. (2010) described the first detailed and dated field evidence of neotectonic activity from a cave in the Northern Calcareous Alps (NCA) and showed that massive flowstones were scratched and ruptured between the last Interglacial and the Early Holocene. They concluded that the nearby Salzach-Ennstal-Mariazeller-Puchberg strike-slip fault (SEMP), which facilitates the extrusion of the Eastern Alps, must be an active fault. The present study supports these earlier findings and investigates liquefaction and complex soft-sediment deformation structures cross-cut by normal faults in the Hirlatz cave. The studied outcrop, which is about 100 km to the west of the studied fault segment of Plan et al. (2010), demonstrates the recurrence of seismic activity in that particular region close the SEMP fault system.

2. Geological setting

The investigated Hirlatz cave is located at the northern rim of the Dachstein karst plateau with a peak elevation of almost 3000 m a.s.l.

* Corresponding author.
E-mail address: Bernhard.Grasemann@univie.ac.at (B. Grasemann).

https://doi.org/10.1016/j.jsg.2018.02.010
Received 1 September 2017; Received in revised form 14 February 2018; Accepted 22 February 2018
Available online 01 March 2018
0191-8141/

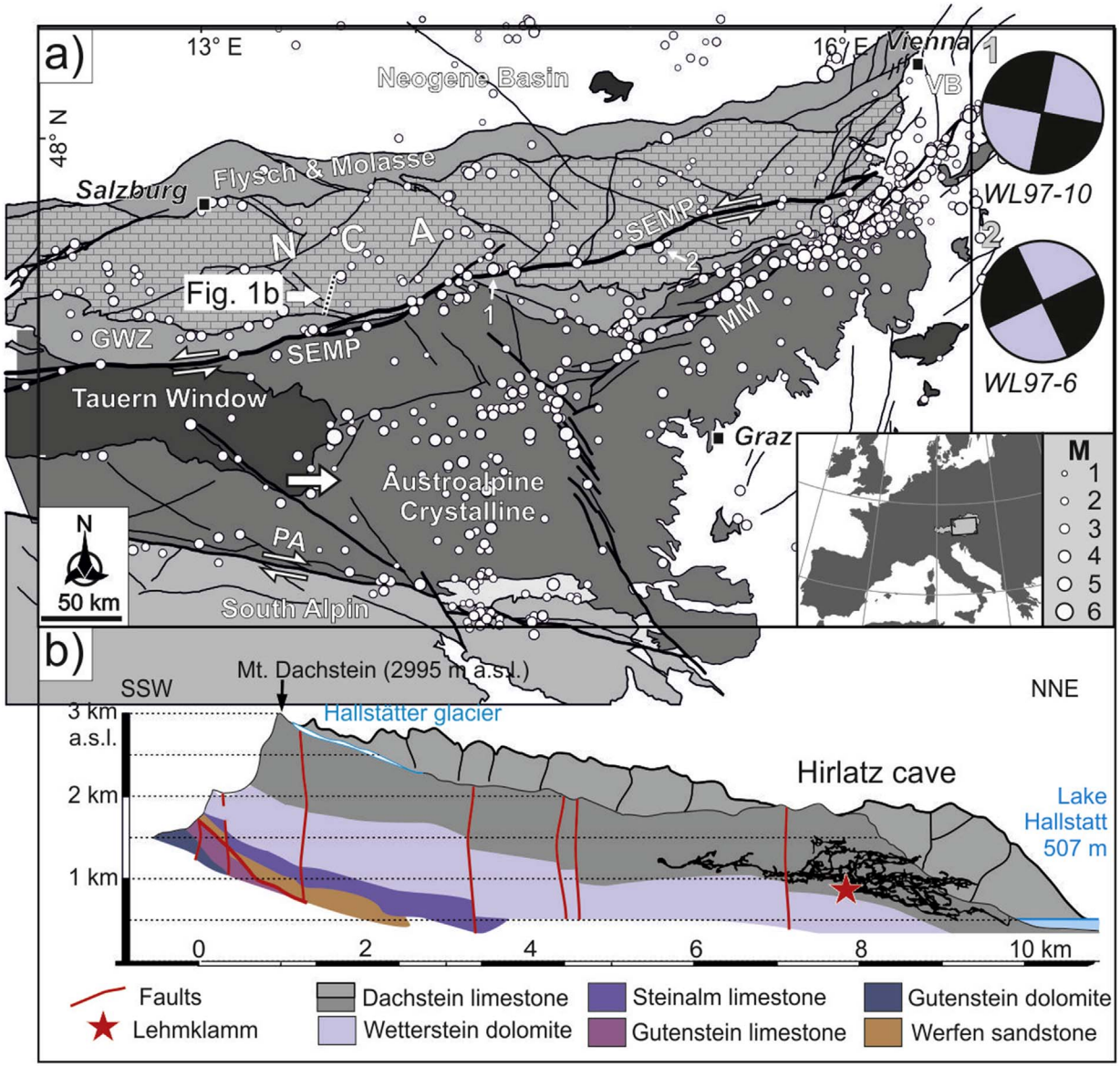

Fig. 1. a) Simplified geological map of the Eastern Alps (SEMP – Salzachtal-Ennstal-Mariazell-Puchberg fault; PA – Periadriatic fault; MM – Mur-Mürz fault; BM – Bohemian Massif, GWZ – Graywacke Zone, NCA – Northern Calcareous Alps; VB – Vienna Basin). White circles indicate epicenters of earthquake events since 1900 (Reinecker and Lenhardt, 1999). The size of the circles is proportional to their magnitude. Single arrow indicates 1.0 ± 0.6 mm/a E-directed movement of GPS station GRMS relative to Bohemian Massif (Grenerczy et al., 2005). Two focal mechanism solutions indicate sinistral strike-slip movement along active segments of the SEMP (Reinecker and Lenhardt, 1999). b) Geological section across the Dachstein plateau (modified after Seebacher, 2016 using Mandl, 1998). Black lines indicate the Hirlatz cave (cave survey data: VH Hallstatt-Obertraun).

(Fig. 1, Pohl and Greger, 2001). The Dachstein massif is part of the NCA, which constitute the uppermost tectonic unit in the Eastern Alps and form a 500 km long and 20–50 km wide thrust belt (Spengler, 1928; Tollmann, 1976). The strata record the history of the Eastern Alpine part of the Tethyan shelf from Permian to Eocene times (Mandl, 2000 and references cited therein). The cave is located in the Upper Triassic Dachstein Limestone formation (Simony, 1847), which represents a distal shallow marine shelf consisting of reef and lagoon facies (Haas et al., 2007). The NCA have been subjected to several tectonics phases, starting with initial nappe stacking in the Upper Jurassic followed by major W-directed thrusting in the Cretaceous. After drowning and deposition of the Upper Cretaceous clastic sediments of the Gosau Group, the NCA were thrusted towards the north into a thin-skinned fold and thrust belt (Frisch and Gawlick, 2003). Sinistral strike-slip movements along the SEMP fault system, which is located along the southern margin of the NCA, commenced in the Miocene and accommodated since then about 60 km extrusion of the central parts of the Eastern Alps towards the Pannonian Basin (Linzer et al., 2002).

The main entrance of the Hirlatz cave is located at 870 m a.s.l. in the Echern Valley, below the 900 m vertical north face of Mount Hirlatz (Buchegger and Greger, 1998; Austrian Cave Register #1546/7). With a length of 105 km and a depth of 1070 m, this karstic cave is the third longest cave system known in Austria. The investigated structures are exposed on a 5.5 m long and 2.5 m high NE-SW striking outcrop wall of cave sediments along a section called *Lehmklamm*, which is located about 2.8 km SE of the cave entrance at 1005 m a.s.l. Fig. 2 shows an orthomosaic of the outcrop, which was created from 24 individual pictures using the photogrammetric software Agisoft PhotoScan Vers. 1.2.4 (www.agisoft.com). Karst hydrological investigations have demonstrated a complex drainage system from the Dachstein plateau through parts of the cave generally directed towards the N, which corresponds to the dip direction of the bedded limestone (Völkl, 1998). At the present time phreatic (completely water filled) and epiphreatic (only filled during floods) conditions are found at different altitude levels within the cave. The investigated sedimentary succession in the Lehmklamm is nowadays located in the vadose zone (water unsaturated

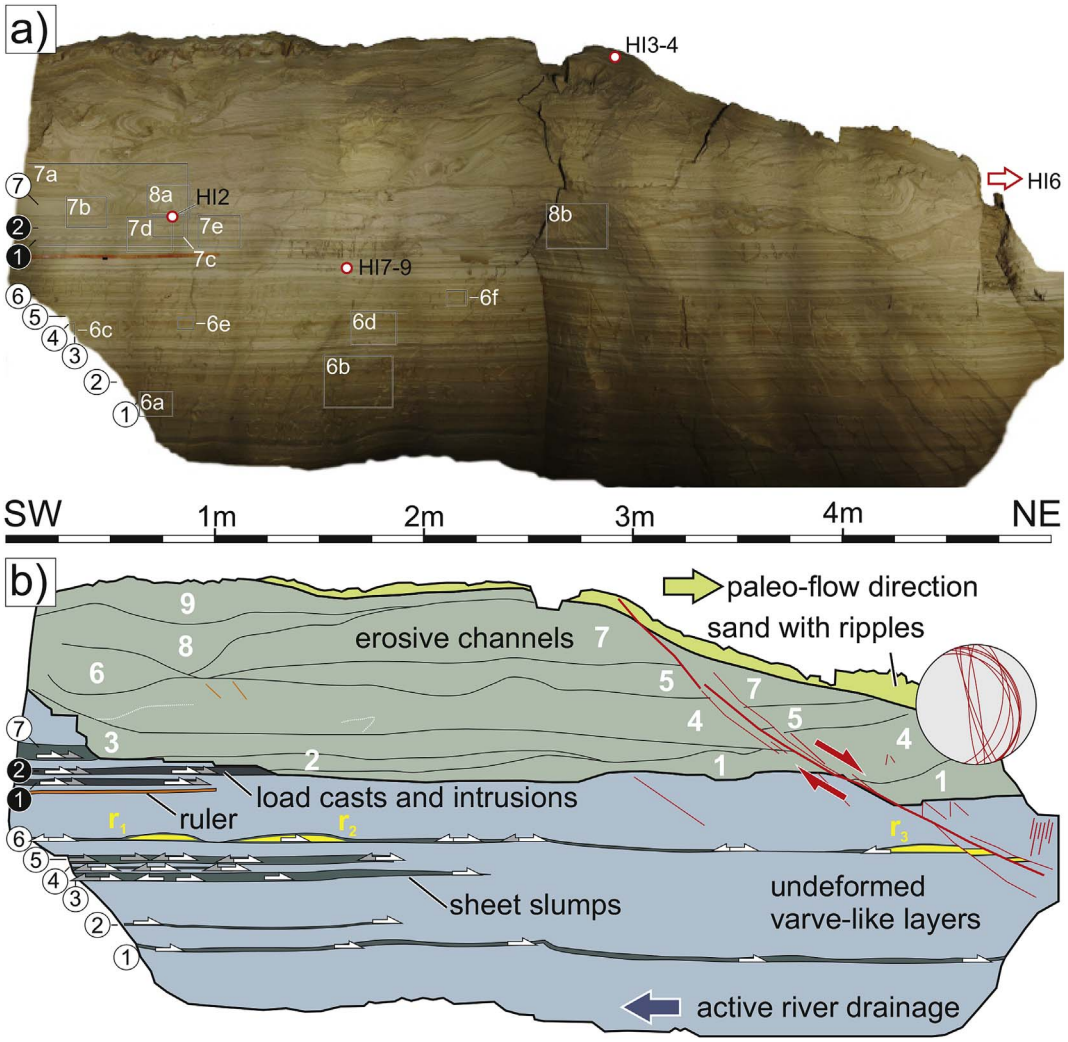

Fig. 2. a) Orthomosaic created from 24 individual pictures of the studied outcrop Lehmklamm in Hirlatz cave (location see Fig. 1). Sheet slumps are labeled 1 to 7 in white circles; layer confined load casts and plastic intrusions are labeled 1 and 2 in black circles. Red circles indicate sampling sites. Black rectangles show locations of details presented in Figs. 6–8. The orange folding ruler has a length of 1 m. b) Line drawing of the orthomosaic. Erosive channels filled with slides are labeled with white numbers 1–9 and r_1-r_3 point to three isolated rafts blocks. Red great circles in the stereoplot represent individual orientations of fault segments and secondary faults. (For interpretation of the references to colour in this figure legend, the reader is referred to the Web version of this article.)

zone) and was eroded sideways by a small active stream flowing to the limestone at the floor of the passage.

3. Description of the cave sediments

The unconsolidated fine grained (clay to silt) sediments at the investigated outcrop within the Hirlatz cave consist of sub-millimeter to several cm-thick layers of dark-brown clay-dominated layers interbedded with light-brown to beige layers with a higher content of silt. Layering is practically speaking horizontal when measured with a standard clinometer (Fig. 3a). In-between the undisturbed layers, nine horizons containing layer-parallel soft-sediment deformation structures occur, which are described in detail below in section 4. The present day surface of the sedimentary succession is a few decimeters below the ceiling of the passage and incised by several erosive channels filled with reworked slides and slumps. Within these channels and at the top of the succession, fine sandy layers with climbing ripples indicate a NE-directed paleo-flow under phreatic conditions, which is opposite to the active vadose drainage towards SW. *Climbing ripples* or *ripples drift cross lamination* indicate rapid deposition during migration of the ripples or if deposition exceeds migration (Sorby, 1859; Allen, 1973). The lee side of the ripples is enriched with dark heavy minerals (Fig. 3b). The provenance of the sediments and the mineralogical difference between the darker and brighter layers were assessed by the heavy mineral content of the silty/sandy layers and the composition and clay content of the bright and dark layers, measured with X-ray diffraction (sample locations are given in Fig. 2a). Sample HI-2 was taken from a fine sandy layer below the erosive channels at the top of the section. HI-3 and HI-4 were sampled from current ripples in silt and sand layers at the very top of the outcrop. Sample HI-6 is from a cm-thick bright calcite-rich layer in the upper section around the NE corner of the studied section. Sample HI-7 was taken from a bright brown silty layer, HI-8 from a brownish clay layer and HI-9 from dark brown clay layers in the central undeformed part of the section.

3.1. Heavy mineral analysis

We used heavy-mineral (detrital minerals having a density that is greater than 2.9 g/cm^3) analysis as a tool to trace the source areas of the investigated sediments. For the heavy mineral analysis, only samples from the silt and sand layers from the upper part of the section were investigated, because the clay layers were almost free of heavy minerals or the grains were too small to be detected in the optical microscope. The samples were decarbonized with diluted acetic acid and a grain size

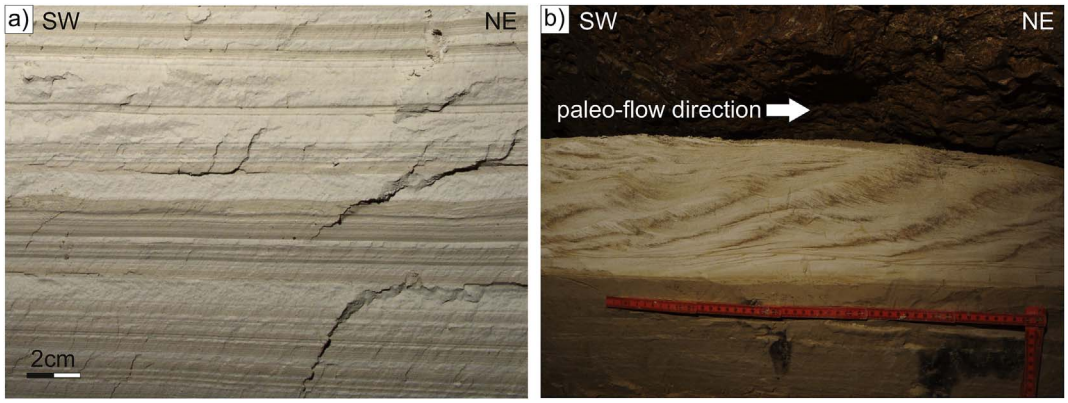

Fig. 3. a) Undeformed section of layered varve-like sediments. b) Climbing ripples on top of the investigated sedimentary succession indicating a paleo-flow towards NE.

from 0.063 to 0.4 mm was used for further analysis. The heavy minerals were separated using 1,1,2,2,-tetrabromoethane ($C_2H_2Br_4$) with a density of 2.94 g/cm^3 at 20 °C. The separated heavy minerals were imbedded in Canada balsam and analyzed under the optical microscope (100–150 grain counts for classification).

Samples derived from the silt and fine-grained sandy layers (HI-2, HI-3, HI4/1 and 2) record a very similar heavy minerals spectrum. The average of all samples returned the following (Fig. 4): Major amounts of epidote (40%), zoesite (21%), zircon (10%) and minor amounts of garnet (7%), chloritoide (5%), rutile (4%), tourmaline (4%), kyanite (4%), apatite (3%) and hornblende (2%). This composition suggests a provenance from a near metamorphic source (see discussion section for more details).

3.2. X-ray diffraction (XRD) analysis

XRD analyses were carried out with a Panalytical PW3040/60 X'Pert PRO diffractometer using copper Kα radiation at 40 kV and 40 mA. All specimens were run at a 2Θ-angle ranging from 2° to 70° (40°) with a step size of 0.0167 and a scanning speed of 5 s per step. For the interpretation the Panalytical X'Pert High score plus software was used (see also Moore and Reynolds, 1997). Details about the sample preparation are given in Appendix A1.

XRD examination of bulk samples showed that the composition of the brighter silt-rich and darker clay-rich layers is very similar, consisting of calcite, quartz, dolomite, ankerite, muscovite, chlorite and biotite and minor amounts of K-feldspar (Fig. 5a). In the darker layers the amount of carbonate is smaller than in the brighter layers and K-feldspar is completely missing. The darker layers contain more mica and the brighter layers are enriched in quartz and carbonates. Also the clay mineral content (< 2 µm, Fig. 5b) is very similar in all measured samples, comprising mainly illite, smectite, chlorite and kaolinite. The bright and dark layers hence only differ in terms of mineral quantities, so that clay minerals are more abundant in the darker layers.

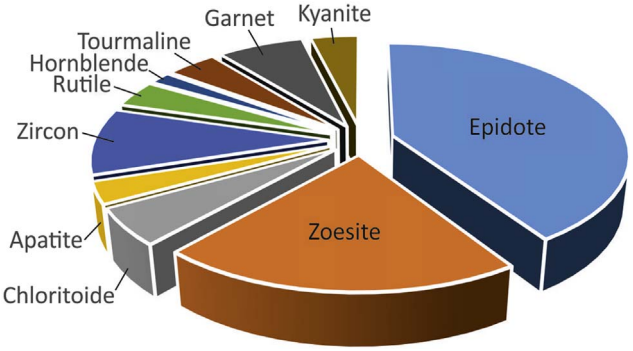

Fig. 4. Averagely the samples (HI-2, HI-3, HI-4/1 and 2) consist of major amounts of epidote (40%), zoesite (21%) and zircon (10%), with minor amounts of garnet (7%), chloritoide (5%), rutile (4%), tourmaline (4%), kyanite (4%), apatite (3%) and hornblende (2%), suggesting a provenance from a near metamorphic source.

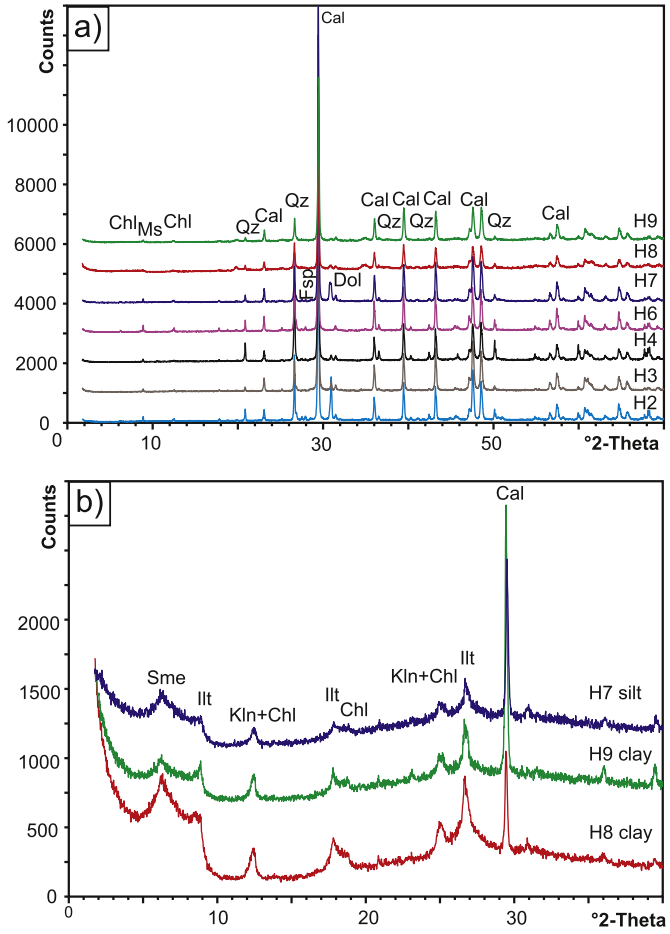

Fig. 5. a) X-ray diffraction patterns of bulk samples. The samples contain calcite (Cal), quartz (Qz), dolomite (Dol), muscovite (Ms), chlorite (Chl) and feldspar (Fsp). b) X-ray diffraction patterns of Mg-saturated clay fractions from samples H7 (silt), H8 (clay) and H9 (clay). Sme = smectite, Ilt = illite, Kln = kaolinite, Chl = chlorite, Cal = calcite.

4. Deformation structures in the sediments

The deformation structures in the investigated sediments, which are generally described as seismites (Seilacher, 1969), encompass soft-sediment deformation structures and normal faults cross-cutting the entire sedimentary succession. Note, that soft-sediment deformation

structures caused by cryoturbation (ice wedge casts, involution) are morphologically very different to the investigated structures (Obermeier, 1996). The soft-sediment structures within the investigated sediments are typical for liquefaction involving the production of regular folds and Rayleigh-Taylor instability of sediment layers within a single sedimentation unit between undisturbed layers (Allen, 1982). During liquefaction water-saturated, unconsolidated sediments are transformed by pressure gradients or shaking from a solid-like to viscous-liquid-like state and are capable of moving on slopes of less than 1° in obedience to body forces forming layer-confined imbricate faults and folds (Lowe, 1976; Owen, 1987; Alsop and Marco, 2011). The investigated soft-sediment deformation structures can be discriminated into four groups (Allen, 1982; Montenat et al., 2007): (i) Sheet slumps with faults and folds and (ii) load casts and plastic intrusions (pseudonodules and ball-and-pillow structures) confined to several cm-thick layers within the undisturbed horizontally sub-millimeter to centimeter laminated varve-like succession. (iii) Erosive channels filled with several erosive slides and slumps of unlithified highly deformed beds. The deformed sediments are overlain by decimeter-thick sands with ripples. (iv) Normal faults cutting through the whole sedimentary succession. In the following, each group is described individually.

4.1. Sheet slumps

Brittle failure, translation and hydroplastic deformation of slump sheets on very gentle slopes can be facilitated by reduction of shear strength due to increased pore fluid pressure in millimeter-to centimeter-thick layered varve-like sediments, which provide clay-rich easy-slip horizons (e.g. Williams and Prentics, 1957; Elliott and Williams, 1988; Strachan, 2002; Alsop and Marco, 2011). The progressive evolution of slump systems include translation along a local slip surface with extension propagating upslope to the head of the slump and shortening propagating downslope towards the toe of the slump (Farrell, 1984; Debacker et al., 2009; Alsop and Marco, 2011).

The investigated outcrop exhibits seven different sheet slumps (labeled 1 to 7 in white circles in Fig. 2) with a thickness of only a few millimeters to centimeters, mostly displaying slump folds and fault-related folds indicating large shortening, although minor extensional structures are locally observed. Only two sheet slumps can be traced along the entire outcrop's length of more than 5 m (1 and 6 in Fig. 2). The other sheet slumps pass laterally into undisturbed strata (2, 3, 4 and 5 in Fig. 2) or are truncated by the erosive channel (7 in Fig. 2). In the following the main characteristics of the individual sheet slumps are discussed in detail:

1) The lowermost exposed sheet slump (labeled 1 in a white circle in Fig. 2) can be traced over the whole outcrop length of 5.5 m and has at the SW side a thickness of c. 2.5 cm that continually decreases to 1 cm at the NE edge of the outcrop. In the SW part, three zones of deformation can be distinguished (Fig. 6a): The bottom and the top of the slump is characterized by zones containing several isoclinal folds with shallow-dipping NE-vergent axial planes, reflecting liquefaction and intense flow. The majority of isoclinal folds cannot be traced over several fold trains, but are sheared-off, forming rootless fold hinges with thinned inverted limbs or coherent vortices. The central zone shows folding of a 4 mm thick bright silt layer. Axial planes of the slumping folds are moderately dipping towards the SW (mean dip direction/dip is 221/19) with shallowly inclined fold axes plunging towards the SE (mean plunge direction/plunge is 161/10), recording an overall NE-vergence of the folds with wavelengths of about 2 cm. The folds are overprinted by a second fold generation (small white arrows in Fig. 6a) with upright axial planes resulting in Type 3 hooks and crescents refold structures. Fold measurements along several 20 cm long transects yielded shortening of c. 60% (assuming that the fold formed by shortening of the layers; see discussion section). In the central part of the outcrop the isoclinal folds in the upper and lower layer of the sheet slump disappear and only the simple NE-vergent folding of the bright silt layer, with wavelengths of c. 5 cm and a shortening of less than 40%, is preserved. Interestingly the antiforms have interlimb angles of c. 30°, whereas the synforms are isoclinal resembling asymmetric billows (Fig. 6b). In the NE part of the outcrop only isolated NE-vergent antiform-synform folds pairs with a spacing of about 50 cm are present. The strata between these fold-pairs are almost undeformed or exhibit open, very low-amplitude folding with a wavelength of about 10 cm.
2) The second sheet slump is only 1 cm thick and can be followed in the SW part of the outcrop for about 1.5 m. Within a dark brown clay-rich layer, a bright 3 mm thick silt layer is either openly folded in linear waves (wavelength c. 3 cm, amplitude a few mm) or sheared in layer-parallel isolated isoclinal antiform-synform fold-pairs resembling asymmetric billows (Fig. 6b). The folded structures are separated by tens of cm's of undeformed layers and the total shortening is less than 10%.
3) Sheet slump No. 3 records a complex polyphase deformation and a significant change of the deformation structures and kinematics from the SW towards the NE: In the SW part of the outcrop layer-bound top-to-SW reverse faults (orange half arrow in Fig. 6c) gradually pass into layer-bound top-to-SW normal faults (white half arrows in Fig. 6c). The deformed layer is about 3 cm thick and the normal faults, with a maximum displacement of less than 5 mm in the layer's center, have a spacing of about 5 mm. The faults have a large displacement gradient, which is accommodated by fault drag and monoclinal folding at the fault tips. As seen from left to right in Fig. 6c, the layer is overprinted by a strong component of layer-parallel shortening resulting in increasingly tighter folding of marker horizons between the normal faults (e.g. dotted white line in Fig. 6c). Further towards the NE this layer passes into a zone of intense folding (Fig. 6d). Deformation is strongly partitioned into fault propagation folding (a_1-a_7) in the lower section comprised of bright 3 mm thick silt layers and a zone of complex folding in an upper clay-rich section with a 1 mm thick silt layer. The slumping direction is clearly towards the NE and the detachment levels of the fault propagation folds are stacked (d_1-d_3) leading to layer thickening from 1.5 cm at the NE side to 2.5 cm at the SW side (Fig. 6d). On the other hand, the fold complexity within the clay-rich layer increases from SW to NE, showing sections of no folding above the antiforms a_7 and partly a_4 and a_5, but intense folding with NE and SW vergence between the antiforms of the fault-propagation folds (e.g. white arrows between a_7 and a_6 in Fig. 6d) where the clay-rich layer is also thickened. Above fault-propagation folds a_1, a_2 and a_3, the clay rich layer is thickened by Type 3 hooks and crescents refold structures (e.g. white arrow between a_2 and a_3 in Fig. 6d).
4) Sheet slump No. 4 displays top-to-the-SW kinematics, which is overprinted by NE-directed shearing at the NE termination of the slump. A spectacular and complex example of this kinematic reversal is shown in Fig. 6e, where SW-directed fault-propagation folds and associated higher order folds f_1 are overprinted by NE-vergent folds f_2. The fault-propagation folds have three different detachment horizons (d_1-d_3) and the marker horizons' offsets range from c. 1 mm to 1 cm. A selection of corresponding hanging wall and footwall cutoffs of some marker horizons (traced with white dotted lines) are marked in Fig. 6e with white circles, whereas orange circles mark the tips of the fault-propagation folds. Earlier folds with the same SW-vergence as the fault-propagation folds (f_1) and the initially NE-dipping fault-propagation folds are refolded by folds with opposite vergence, resulting in Type 3 hooks and crescents refold structures. Truncations of marker horizons (white arrows in Fig. 6e) clearly demonstrate that sheet slump No. 4 has been partly eroded prior to later sedimentation. Note that the surface morphology of the slump was filled by later sediments, leading to layer thinning above the culminations and layer thickening above the

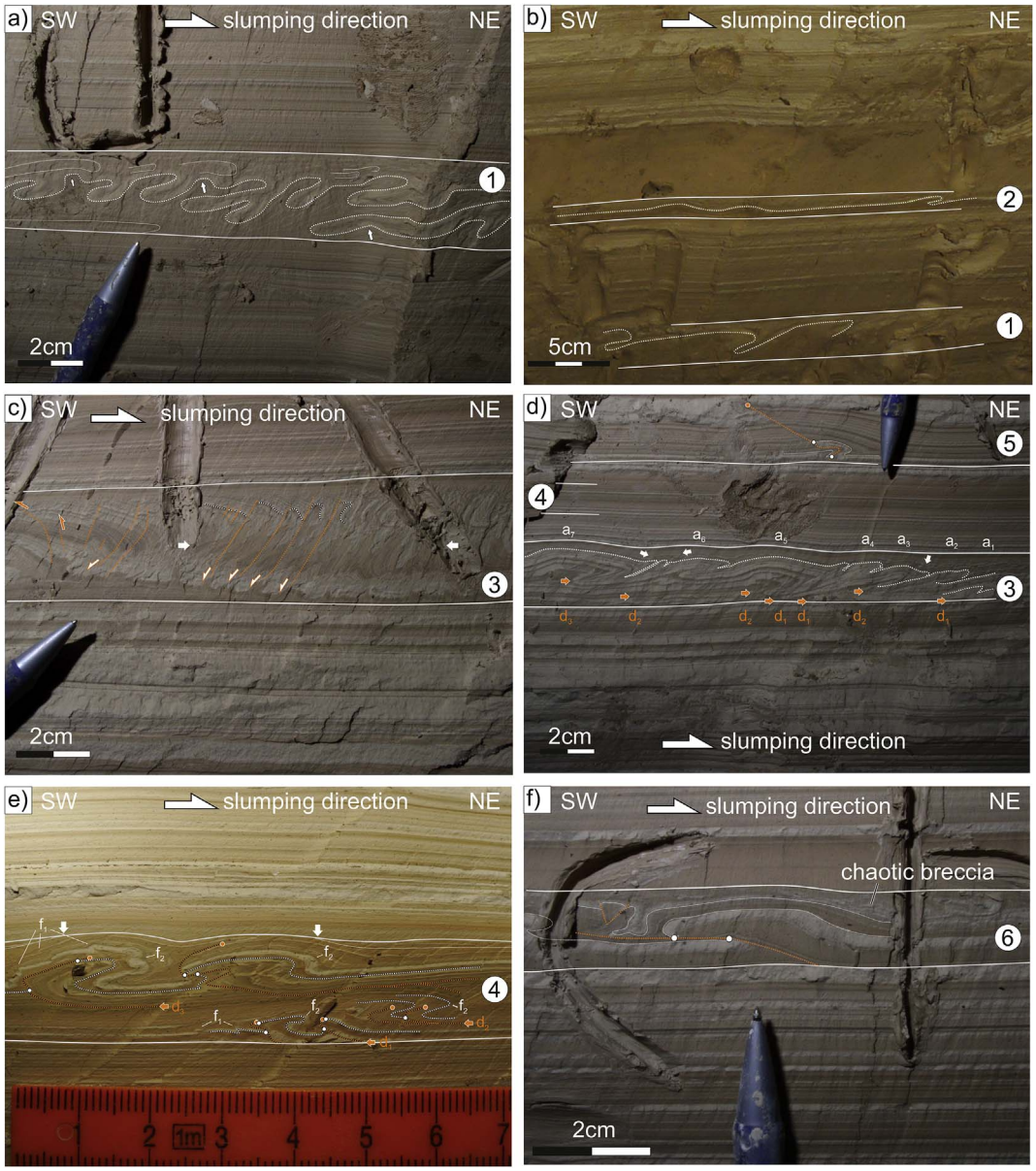

Fig. 6. a) Intense NE vergent folding in sheet slump No. 1. Note second fold generation with upright axial planes (white arrows). b) NE vergent folding in sheet slump No. 1 and folds in sheet slump No. 2, which are separated by almost undeformed layers. c) Domino boudinage overprinted by NE directed shearing resulting in extremely deformed flanking structures in sheet slump No. 3. d) Fault-propagation folding above three different detachments levels (d_1-d_3) in sheet slump No. 3. SW directed fold propagation folding overprinted by ductile NE vergent folding in sheet slump No. 5. e) SW vergent fault-propagation folding and associated higher order folds (f_1) above three different detachments levels in sheet slump No. 4 (d_1-d_3), overprinting NE vergent folding f_2. Note the erosive contact to the overlying undeformed layers (white arrows). f) Fault propagation folds with opposing vergence. Note that the bathymetric synforms are filled with a chaotic breccia.

troughs. Sheet slump No. 4 can be only traced for c. 1 m and the corresponding layers towards the NE appear completely undeformed (see layer 4 labeled in Fig. 6d).

5) Sheet slump No. 5 can be traced for 2 m; its continuation towards the NE is completely undeformed. The structures record an earlier top-to-the-SW kinematics overprinted by top-to-the-NE movement, similar to sheet slumps No. 3 and 4. In the earlier deformation phase, SW-vergent fault-propagation folds developed within a 1.5 cm thick brownish sub-millimeter varve-like layer and propagated into a 1 cm thick silt layer (orange circle indicates the fault tip in Fig. 6d). The hanging wall and corresponding footwall cutoffs (white circles in Fig. 6d) display displacements in the order of 1 cm. The distance between the regularly spaced fault propagation folds is c. 10 cm. Within the basal layers, the SW-vergent fault-propagation folds are refolded by NE-vergent folds.

6) Sheet slump No. 6 has a thickness of 1.5 cm and consists of a 3 mm thick bright silt layer embedded within a 1 cm thick brown more clay-rich layer. The sheet slump is exposed along the entire outcrop and both fault-propagation folds and box-shaped detachment folds with SW and NE vergence are present (Fig. 6f). Shortening, determined along a 1 m long transect, is in the order of c. 50%. Above these structures a 0.5 cm thick unit comprised of mm-thick layers exhibits complex folds, which are partly dismembered or even chaotically brecciated. This sheet slump contains three c. 2 cm thick isolated raft blocks (r_1-r_3 in Fig. 2) comprised of mm-layered sediments with internal normal faults. The term *raft* is used here to describe allochthonous fault blocks above a detachment that were separated beyond mutual juxtaposition (Burollet, 1975). The raft-internal and raft-bordering normal faults dip towards the SW and NE. Interestingly, the base of raft r_2 is overprinted by NE-vergent

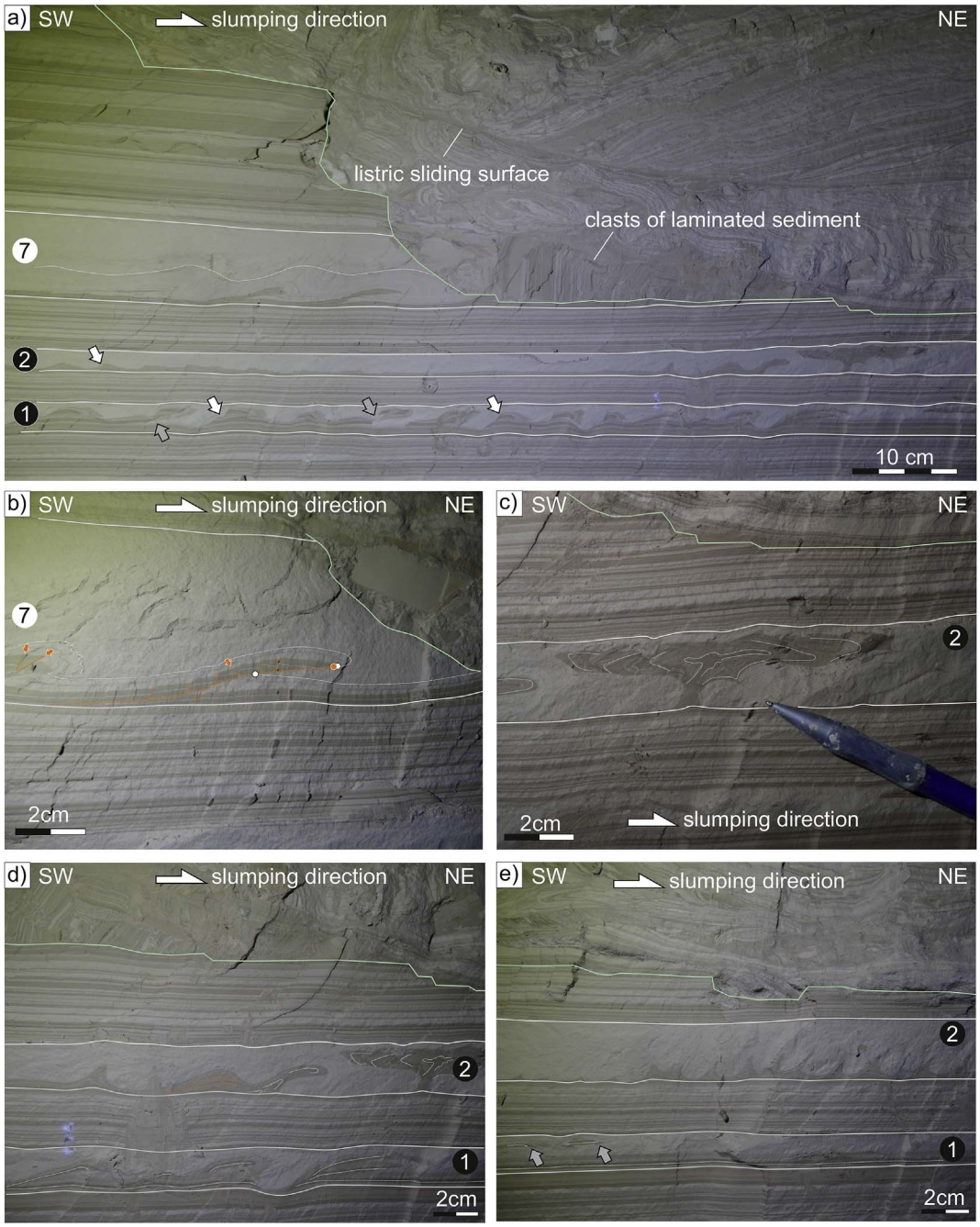

Fig. 7. a) Layers 1 and 2 with load casts and plastic intrusions. Sheet slump No. 7 with NE vergent fault-propagation folding overprinting earlier formed normal faults. Erosive channels filled with slides. b) Detail of sheet slump No. 7 with NE vergent fault-propagation folding. c) Detail of mushroom shaped intrusion. d) Layers 1 and 2 with load casts and plastic intrusions overprinting earlier sheet slumps. e) Slightly NE inclined flame structures in layer 2 with load casts and plastic intrusions.

folds, whereas the base of raft r_3 is overprinted by SW-vergent folds.

7) Sheet slump No. 7 is only exposed for 50 cm due to truncation by erosive channels (Figs. 2 and 7a). It consists of a basal 0.5 cm-thick dark and fine grained layer that was thrusted and pushed into a 4.5 cm thick bright coarse grained silt layer, which accommodates this intrusion and shortening by folding (Fig. 7b). The displacement on the thrusts is about 2 cm. Several 0.5 cm spaced locally conjugate normal faults within the darker layer at the base of this sheet slump manifest extension prior to thrusting. The normal faults are present in both the thrusts' hanging wall and footwall, but only the faults within the hanging wall were reverse-reactivated during thrusting (orange arrows in Fig. 7b).

4.2. Load casts and plastic intrusions (convolute bedding, pseudo-nodules and ball-and-pillow structures)

Load casts and plastic intrusions, which are the result of Raleigh-Taylor gravitational instabilities of liquidized layers with denser sediment superimposed on lighter sediments (Allen, 1982), are confined to two, c. 2 cm thick layers within the otherwise undisturbed laminated succession (labels 1 and 2 in black circles in Fig. 2 und 7a, c, d, e). Interestingly, in both layers the gravitational instabilities are superimposed on earlier sheet slumps in which the laminated finer grained darker lower layer exhibit thrusts, duplex structures, fault-propagations folds and folds with NE-directed kinematics (Fig. 7a and d). Although the contact to the overlying coarser grained white silt is strongly

overprinted by the gravitational instabilities and intrusions, an erosional contact is clearly preserved (examples are indicated by white arrows in Fig. 7a). The majority of these structures developed along the interface between a lower fine-grained dark layer and an upper coarse-grained white silt layer (Fig. 7d and e) and can be classified as load structures (Allen, 1982), showing bulges, deep or rounded sacks, irregular protuberances or diapirs drawn out into long streaks (flame structures in the sense of Kelling and Walton, 1957). The contacts frequently exhibit a cuspate-lobate form, which consistently points its rounded surface (lobes) into the darker clay-rich layer and its acute surface (cusps) into the white coarser silt layer. Cusps always point towards the material with the higher effective viscosity in relation to the adjacent layer at the time of deformation (Ramsay and Huber, 1987). Although cuspate-lobate structures have been described from mechanically layered metamorphic rocks where their development is favored by low viscosity contrast and non-linear fluids (Fletcher, 1982), which experienced layer-parallel shortening, their morphology is similar to that of alternating load casts and flame structures in sedimentary sequences (Haneberg, 1991). Many of the observed structures are not symmetrical but lean significantly towards the NE, consistent with the inferred slump direction (Fig. 7e). In some cases the brighter silt layer did not only sag into the underlying clay-rich laminated layer, but intruded along fault planes formed during the earlier sheet slumping event, resulting occasionally in dismembering of thrust sheet pieces and duplex structures (e.g. grey arrows in Fig. 7a and e). Some spectacular diapiric intrusions even preserved the internal lamination of the laminated clay-rich layer, which closely follows the external form of the diapir (e.g. the head of the mushroom shape and the strongly inclined diapir in Fig. 7c and d).

4.3. Erosive channels

The uppermost part of the exposed section is cut by an erosive channel that removed about 0.5 m of the laminated sediments containing the layer-parallel soft-sediment deformation structures described above. The channel is filled with nine distinct erosive slumps, which are overlain by decimeter-thick laminated varve-like layers and sands with ripples. The erosive slumps have the following characteristics: (i) They have an erosive basis that can be comprised of a listric sliding surface (Fig. 7a), or cm-sized clasts derived from the underlying layered sediments (Fig. 7a), or “exotic” red clay clasts not exposed in the underlying section (Fig. 8a, c), and/or white rippled sands with dark minerals accumulating at the lee side of the ripples (Fig. 8b). (ii) They are internally structured and consist of several highly deformed smaller slumps, sediment blocks or slides exhibiting internal preservation of sedimentary structures.

Within the slumps the sedimentary layering is deformed into folds, complex refold structures (Type 2 mushrooms and Type 3 hook and crescents, Fig. 8b). Locally, folding lead to the formation of a well-developed crenulation lineation (mean plunge direction/plunge is 190/05) that is sub-parallel to the fold axes (Fig. 8b). Some slumps also exhibit normal faults indicating local extension. The slides preserve not only the internal varve-like layering, but also layer-parallel soft-sediment deformation similar to the underlying sediments. The internal layering of the individual slides sharply terminates at faults, along which the slides were translated from their initial position. A pronounced reverse drag and local changes from reverse to normal drag along the bounding faults indicates that the slides were displaced from their original position along rotating normal faults (i.e. reverse drag a-type flanking folds; Grasemann et al., 2003).

The lowermost slump in the erosive channel consists of a silt matrix with reworked and completely dismembered deformed sediments. In addition to the aforementioned “exotic” red clay clasts, isolated rootless folds and refolded packages are preserved (Fig. 8c). Although the majority of the slumps record chaotic structures with dismembering of individual internally deformed sediment blocks, the vergence of some slump folds suggest that the majority of slumps derived from the SW side of the outcrop and translated towards the NE (e.g. slump 3 in Figs. 2 and 8b). Some slumps may have slid into the channel from the opposite side (e.g. slump 1, Figs. 2 and 8a). A particularly clear example indicative of the sliding direction is preserved in the SW part of slump 4 (Fig. 2), where a coherent package of laminated sediments is shortened and folded on the NE-side and extended on the SW-side, a structural zonation consistent with models for slump sheet translation above an underlying detachment with contraction at the toe and extension at the head of the slumps (Farrell, 1984).

The slump pile within the erosive channel is sealed by several cm-thick successions of mm-thick alternating clay and silt layers and several cm-thick rippled sand layers, indicating paleo-flow directions towards the NE, which is in fact opposite to the current drainage direction (Fig. 3b). Note that the accumulation of black, heavy mineral rich layers on the lee-side of the ripples shown in Fig. 3b was used for the heavy mineral spectrum analysis.

4.4. Normal faults

The described sedimentary section filled up almost the entire passage (Fig. 8d). A major NE-dipping normal fault (mean dip direction/dip is 074/29) with a maximum displacement of c. 40 cm cuts through the entire sedimentary succession and represents the youngest deformation in the studied outcrop. This normal fault can be traced as a sharp fault plane (red line in Fig. 8e), but is in detail comprised of a c. 5 cm wide zone of intense faulting, suggesting that the fault formed by the linkage of en échelon Riedel and P shears. Within a 1 m wide halo (or damage zone) around the main fault (or principal displacement surface), numerous syn- and antithetic secondary Riedel faults with displacements ranging from a few mm to cm are present, both within the hanging wall and the footwall. These non-layer bound faults only developed adjacent to this normal fault zone and are absent in other parts of the exposed section. Notably, the principle displacement surface intersects the top of the sedimentary succession exactly where a brittle fault with polished slickensides and a dip-slip lineation (Fig. 8f) offsets the passage by c. 10 cm (Fig. 8d).

5. Discussion

5.1. Depositional environment and source of the sediments

The investigated sediment type is very common in caves of the central NCA and represents frequently the topmost or youngest strata. Seemann (1973), who investigated the sediments of the neighboring Dachstein-Mammut cave, termed it *Heller Höhlenton* (bright cave clay). There the calcite content varies between 57 and 67% (Franke and Ilming, 1963). Already Spöcker (1925) proposed stagnant conditions during sedimentation. It is generally accepted that the cave sediments are a deposit of glacial meltwaters that were rich in abraded limestone particles (e.g. Schauberger, 1957; Audra et al., 2002). The stagnant depositional conditions and the risen karst water table can be explained by Pleistocene back flooding (Ford and Williams, 2007): During glacial high stands, the valley was filled by the over 1 km thick Traun glacier that blocked the springs, causing flooding of elevated cave passages. Since the studied strata are topmost and flooding of this part of the cave occurred during the last glacial maximum, a depositional age of c. 25 ka is most likely. The syn-sedimentary liquefaction processes and soft sediment deformation would be hence of the same age.

The investigated fine grained cave sediments, which were not affected by soft sediment deformation, consist of sub-millimeter to several cm-thick horizontal layers. The mineralogical composition of the brighter silt-rich and darker clay-rich layers is very similar (Fig. 5). The brighter layers contain more carbonate and quartz grains, whereas the darker layers contain no K-feldspar and are enriched in clay minerals (especially illite). It is very likely that the layering represents annual

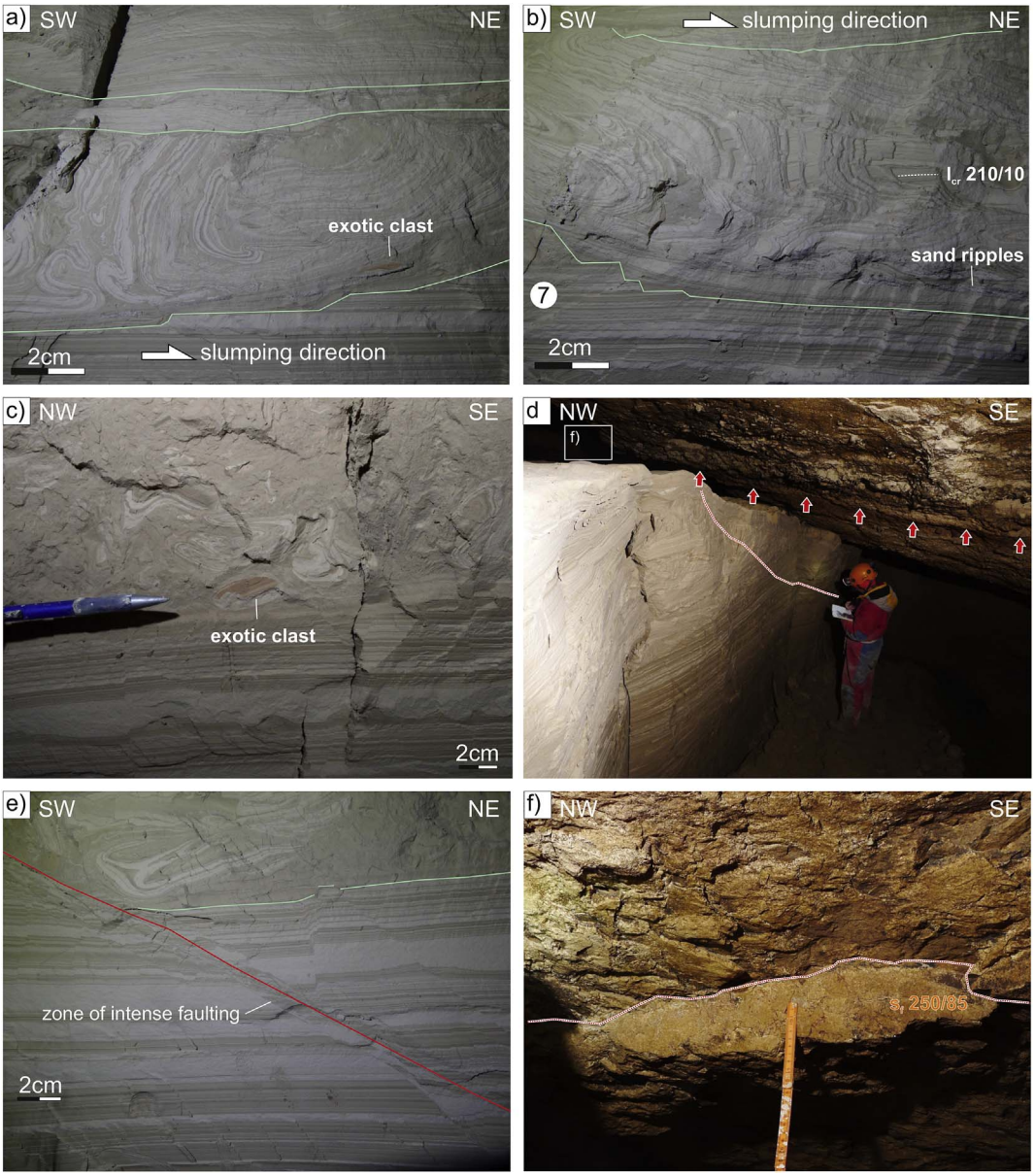

Fig. 8. a) Details of a slide with complex refold structures in the erosive channels. Note the exotic clasts at the base of the channel. b) Folds with crenulation cleavage in a slide within an erosive channel. Note the sand ripples at the base of the channel. c) Details of a chaotic breccia with exotic clasts at the base of an erosive channel. d) Normal fault cutting the entire investigated section (red dotted line). Fault offsetting the gallery (red arrows). e) Close-up of ENE dipping normal fault. f) Details of fault offsetting the passage. (For interpretation of the references to colour in this figure legend, the reader is referred to the Web version of this article.)

varve-like deposits (Spöcker, 1925; Audra et al., 2002): The brighter, coarser grained layers were deposited under higher energy conditions when meltwaters carried sediment into the cave during spring and summer. During winter, when water and sediment supply was reduced, finer grained sediment was deposited forming the darker layers.

If the dark-bright layer couples represent varves, then the total number of layer couples represents the time span of sedimentation in years. The mean sedimentation rate in millimeters per year is hence obtained by dividing the sediment thickness by the varve count. The calculated sedimentation rate at different sections across the exposed undeformed sediments yielded values ranging from 1.7 to 6 mm/a. Disregarding possible disconformities and thickness changes of the sediment pile due to sheet slumping, a maximum sediment thickness of about 3 m, measured on the cave wall opposite to the investigated outcrop, where erosive channels are absent, indicates that deposition of the strata occurred in a time span of 0.5–1.8 ka.

Heavy mineral analysis of four samples shows a predominance of epidote and zoisite and smaller amounts of kyanite, garnet and chloritoid (Fig. 4). These minerals indicate that certain sedimentary volumes were derived from a metamorphic source, probably characterized by high-pressure and greenschist metamorphism. The source rock of the heavy minerals could therefore be the Paleogene metamorphic Penninic domain in the Tauern Window and/or the Variscan to Eoalpine polymetamorphic rocks of the Austroalpine Crystalline or, more specifically, the Koralpe-Wölz nappe system of the Adriatic domain (Schmid et al., 2004), both of which are nowadays located S of the NCA. The modern drainage system of the Dachstein massif (peak range in the south of the plateau is above 2500 m a.s.l.) through the Hirlatz cave is completely separated from the southern metamorphic domains by the SEMP and the deeply incised Enns valley (about 700 m a.s.l.) and is therefore incapable of transporting sediments from a southern crystalline source into the cave. However, the Dachstein plateau represents a Late Eocene/Early Oligocene paleosurface, which was covered by at least 1 km thick terrestrial gravels and sands of the Augenstein Formation in

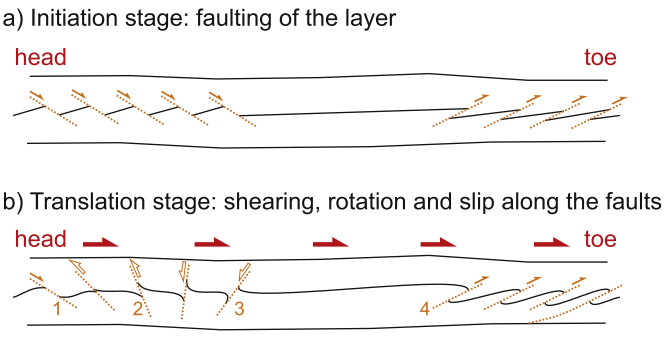

Fig. 9. Conceptual model for the formation of intensely deformed flanking structures in sheet slump No. 3 (compare with Fig. 6c). a) Initiation stage: faulting of the layer with oppositely dipping normal and thrust faults at the head and toe of the slump, respectively. b) Translation stage: shearing, rotation and slip along the faults and formation of a-type and s-type flanking folds at the head and toe of the slump respectively.

Oligocene times (Frisch et al., 2001). The Augenstein Formation consists mainly of polycrystalline quartz derived from metamorphic rocks of the Austroalpine Crystalline. Although sedimentation of the Augenstein Formation ceased in the Early Miocene, followed by erosion and uplift of the Dachstein paleosurface at c. 10 Ma, mostly allochthonous remnants of the Augenstein Formation are still found all over the plateau and in caves (Frisch et al., 2001). The Augenstein Formation and its weathering products are hence the most likely source for the heavy minerals sampled in the Hirlatz cave sediments.

5.2. Sheet slump geometries

The following discussion focuses on the geometry of the sheet slumps (labeled 1 to 7 in white circles in Fig. 2) and not on the erosive channels filled with slides and slumps on top of the investigated sedimentary succession. The latter have an erosive base filled with sand ripples and exotic clasts and their origin is, in our opinion, not seismically triggered, but gravity driven, induced by the incision of the gradually developing stream course.

The majority of the studied soft-sediment structures are associated with sheet slumps that were emplaced following liquefaction and gravitationally induced downslope translation over a substantial distance of a superficial layered deposit, which either failed by viscous flow folding or by slip surface development (Allen, 1982). Although some authors emphasize the chaotic nature of structures within slump systems (Davis et al., 1996), the orientation of the slump fold hinges, which are characteristically normal to the downslope direction (Jones, 1939), is typically used to infer the palaeoslope dip direction (see Alsop and Marco, 2012a and references cited therein). Normal faults, thrust faults and fault related folds are also thought to reflect the orientation of the palaeoslope on the basis of a simple model, in which slump translation along a detachment is accommodated by upslope propagating extension at the head and downslope propagating contraction at the toe of the slump (see reviews in Woodcock, 1979; Maltman, 1994; Strachan and Alsop, 2006; Debacker et al., 2001; Waldron and Gagnon, 2011). During progressive development of slump systems four end-members of structural cross-cutting relationships within the slump may be observed (Alsop and Marco, 2011): Structures at the head may record either progressive extensional structures or, if the system locks first at the toe, extensionally overprinted contractional structures. Conversely, structures at the toe may record either progressive contractional structures or, if the system locks first at the head, contractionally overprinted extensional structures.

The folds and fault-related folds as well as the asymmetry of the load structures within the investigated sheet slumps suggest that the slumps slid towards the east. Furthermore, the majority of sheet slumps are only present in the SW-part of the outcrop's face, where they record significant shortening and can be traced into undeformed layers when traced towards the NE (Fig. 2). We therefore deduce that the investigated section exhibits the slump toes, whereas the slump heads, presumably located further towards the SW, are not preserved. Several slumps record complex overprinting structures, which are discussed below.

Sheet slumps No. 1 and 2 record a consistent fold vergence suggesting a transport direction towards the E. Local refolding resulting in Type 3 interference patterns (Fig. 6a) probably did not form by two oppositely vergent folding phases, but are thought to have formed by shearing of initial folds (Alsop and Marco, 2013) and intense progressive shortening during the slumps' cessation stage and lock-up (Alsop and Marco, 2011).

Sheet slump No. 3 is more complex and records in its SW-part shallowly NE-dipping normal faults, which gradually pass into steeply NE-dipping thrusts and SW-dipping normal faults (Fig. 6c). The same layer exhibits in its NE continuation NE-vergent folds and fault propagation folds with multiple internal detachment horizons (Fig. 6d). We explain this structural style with the following conceptual model, summarized in Fig. 9: (i) During slump initiation, layer-bound normal and reverse faults form at the head and toe of the slump, respectively (Fig. 9a). (ii) The translation stage is controlled by non-coaxial gravity driven down-slope movement and internal shearing of the slump. Faults dipping shallowly to the slumping direction (i.e. towards NE) are reactivated as normal faults, reflecting the geometry of extensional shear bands (1 in Fig. 9b; Passchier, 2001; Grasemann et al., 2003). During progressive shearing faults may rotate into a steeper orientation, resulting in reverse faults with reverse drag a-type flanking folds (2 in Fig. 9b). Further shearing may even overturn the faults, leading to normal faults with reactivation of the structures as reverse drag a-type flanking folds (3 in Fig. 9b). Thrusts, initially dipping oppositely to the slumping direction, develop normal drag s-type flanking folds (4 in Fig. 9b), which may further develop into fault propagation folds (Fig. 6d; Wiesmayr and Grasemann, 2005).

Sheet slumps No. 4 and 5 record very complex structures because top-to-SW thrusts and fault-propagation folds are overprinted by NE-vergent folds (Fig. 6d and e). Similar to sheet slump No. 3 different internal detachment levels are present within the same slump (d_1-d_3 in Fig. 6e). In order to highlight the complex structure shown in Fig. 6e, the faults forming fault-propagation folds are traced with orange dotted lines and their fault tips are marked with orange circles. Hanging wall and footwall cut-offs of selected marker layers (white dotted lines) are indicated with white circles. We presume that only the toes of slumps No. 4 and 5 are exposed, since all structures formed due to contraction and the slumps can be traced towards the NE into undeformed layers. Fig. 10 hence illustrates the conceptual model derived for the slumps' toe sections only. Interestingly, the earlier stage of deformation (grey half arrows in Fig. 2) is characterized by thrusts, fault bend folds or fault propagation folds with top-to-SW, i.e. upslope verging, kinematics (Fig. 10a). Within slide No. 5 (not in No. 4) the kinematic changes to downslope thrusting at the SW termination of the section. We interpret these upslope-directed thrusts as back-thrusts and folds, which can develop during contraction at the slump's toe (Alsop and Marco, 2011), where material moves down slope and underthrusts the arrested sediments (“downslope-directed underthrust model”; Alsop et al., 2017a). During downslope sliding of the slump layer-parallel shearing (Alsop and Marco, 2011) is overprinting earlier structures, resulting in rotation and shear folding of earlier folded layers and/or folding of earlier developed thrust planes with opposite vergence, i.e. SW-vergent folds f_1 are overprinted by NE-vergent folds f_2, which also fold the thrusts (Fig. 10b).

Sheet slump No. 6 extends along the entire studied section and is the only slump containing rafts (r_1-r_3 in Fig. 2), which are separated over a distance of more than 2 m. Internally the rafts reveal extension accommodated by downslope-dipping normal faults, but the layers between the rafts exhibit contraction in the form of box folds and oppositely vergent folds, blanketed by intensely brecciated and

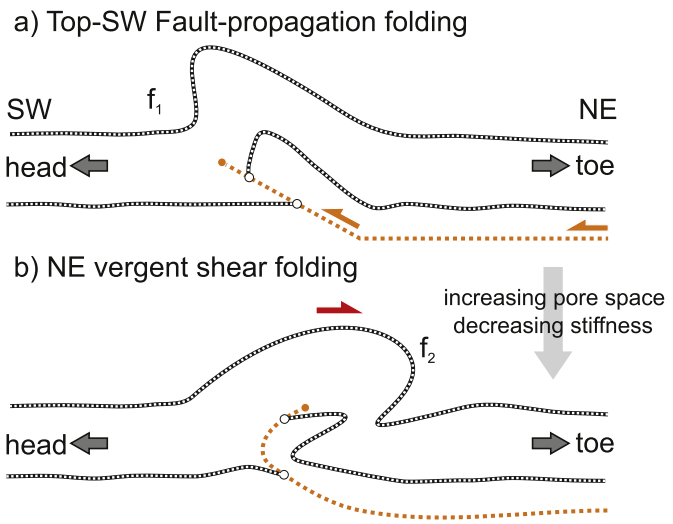

Fig. 10. Conceptual model for the formation of folded fault-propagation folds with opposite vergence (compare with Fig. 6d and e). a) Top SW fault-propagation folding. b) NE vergent shear folding.

dismembered layers. While all other sheet slumps contain coherent or semi-coherent volumes, the exposed section of sheet slump No. 6 could either represent an intensely deformed incoherent slump portion (Alsop and Marco, 2013) or could alternatively be interpreted as a flow slide (Allen, 1982). We hypothesize that the rafts were separated from their (unexposed) source layer by extension and subsequently slid down the paleoslope, eventually coming to rest leading to significant shortening and dismembering of the inter-raft strata.

Due to incision of the erosive channels, sheet slump No. 7 is only exposed for less than 0.5 m. Normal faulting of the darker basal layer was followed by thrusting of the fractured layer, piercing into the brighter layer above, which accommodated shortening by intense NE-vergent folding.

In summary, our observations suggest that the preserved outcrop displays the toes of individual slumps, whereas the heads were located further to the SW, where the cave sediments were eroded. Frequent observations of thrusts overprinted by folding suggest that *contractional translation* was followed by *contractional cessation* (Alsop and Marco, 2011) and therefore indicate that only the slumps' toes are preserved. Although the deformational style of certain layers within a slump is often lithologically controlled, with folding tending to develop in lithologies more susceptible to viscous deformation and thrusting in lithologies more prone to brittle deformation (Alsop and Marco, 2011), several of the studied sheet slumps record evidence for an earlier stage of faulting followed by a stage of ductile shear folding, a temporal deformational style change that has also been reported from other areas (Alsop and Marco, 2014). We hypothesize that this style change is due to a change of mechanical properties during sliding. It is likely that the pore space between the initially densely packed grains increased (dilation) during sliding, leading to a decrease of the layer's stiffness. Stability analysis of the shortening of an elasto-plastic layer on a viscous substratum (see overview by Leroy and Triantafyllidis, 2001) indicates that the structural mode (faulting vs. folding) during incipient failure depends, amongst other factors, on the stiffness of the brittle layer, i.e. a stiff layer fails by faulting rather than folding.

5.3. Seismic origin of the sheet slumps and liquefaction structures

Sheet slumps may be caused by high sedimentation rates leading to pore fluid pressures that can be in excess of hydrostatic which effectively weakens the sediments. Alternatively, steepening of the surface slope by for example fault block tilting can initiate slumping (Gibert et al., 2005). In case of the investigated sediments in the Hirlatz cave both processes can be excluded because sedimentary layering is still sub-horizontal and the varve-like nature of the sediments indicates a low energy environment with relatively low sedimentation rates. Then again soft sediment deformation structures like load casts or involutions may be related to frost-and-thaw instabilities on a gentle slope (Vandenberghe, 1988). In fact the morphology of folds, flames, pillows and pseudonodules formed due to frost action can mimic those formed by seismic shock (Horváth et al., 2005). However, cryoturbation produces mainly infilling of sediments from above and is associated with platy, lenticular structures indicating frost action on the uppermost part of the sediments (Obermeier, 1996; Moretti, 2000). Such structures are not exposed in the investigated sediments of the Hirlatz cave and we therefore conclude that seismically triggered shaking leading to liquefaction and the built-up of a high pore-fluid pressures, resulting in dramatically reduced shear strength (Allen, 1982), is the most plausible cause for the origin of the observed sheet slumps. This conclusion is supported by the exposure of an active fault scarp, which must postdate the age of the passage (Fig. 8d and f). Although a coincidental alignment of the scarp with the normal fault within the soft-sediments cannot be excluded, this observation indicates active tectonics in the vicinity of the studied outcrop. Since we deduced that the sediments are of glacial origin and that phreatic conditions were caused by glacial back flooding during the high-stand of the last glaciation, earthquakes induced by glacial rebound are unlikely. Interestingly, very similar soft sediment deformation structures caused by seismotectonic activities were described from the Sous les Sangles cave in the Jura Mountains in France (Lignier and Desmet, 2002).

There is abundant evidence for long-lived movement and associated seismicity along the still active SEMP strike-slip fault system located just south of the Dachstein massif (Reinecker and Lenhardt, 1999; Grenerczy et al., 2005; Frost et al., 2009; Plan et al., 2010; Schröckenfuchs et al., 2015). Interestingly, a brittle fault surface with polished slickensides, offsetting the passage by c. 10 cm, is exposed directly above the investigated cave sediments. Liquefaction, which is generally considered to be related to earthquake activity (Allen, 1982), is furthermore supported by the presence of load casts, intrusions and flame structures (Fig. 7c, d, e). We therefore propose that the observed sheet slumps and liquefaction structures are associated with seismic activity along the nearby SEMP fault system.

Although the quantification of earthquake intensities based on the size of observed ground effects such as landslides, ground cracks and liquefactions, is highly problematic, especially if the regional distribution of the effects is unknown (Tuttle, 2001; Martino et al., 2014), it is tempting to speculate about magnitudes and intensities of the earthquakes that generated the observed structures. Based on the Italian catalogue of liquefaction and the Italian seismic catalogue, the triggering events for liquefaction range from intensities (MCS) V to XI and from magnitudes (Ms) 4.2 to 7.5 (Galli, 2000). Even earthquakes with an intensity of V can cause liquefaction within a radius of 10–15 km to the epicenter. According to the Environmental Seismic Intensity Scale 2007 of the International Union of Quaternary Research (INQUA), intensities with at least IV-VI are required for creating liquefaction in fine grained sediments within a layer of a thickness of up to 3 cm (Michetti et al., 2007).

Linear waves, billow-like asymmetric folds and coherent vortices in slump No. 1 and 2 (Fig. 6a and b) strongly resemble structures produced by shear instabilities of stratified layers due to relative sliding via the Kelvin–Helmholtz instability mechanism triggered by earthquake shaking (Heifetz et al., 2005). The intensity of such soft sediment deformation is a function of layer thickness and ground acceleration. The majority of observed structures within the c. 2 cm thick slumps No. 1 and 2 are linear waves and asymmetric billows, corresponding to a peak ground acceleration of 0.1–0.3 g or intensities between VI-VII (Wetzler et al., 2010).

If one accepts the seasonal origin of the dark and bright layered sediments and the derived sedimentation rates (discussed in Section

Table 1
Calculated time spans of sedimentation for the undisturbed layers between the sheet slumps (1–7 in white circles in Fig. 2) and the load casts and plastic intrusions (1–2 in black circles in Fig. 2) for estimated sedimentation rates of 1.7 and 6 mm/a respectively.

layers with soft sediment deformation	distance between layers [mm]	time [a]	
		1.7 mm/a	6 mm/a
① - ②	60	35	10
② - ③	200	118	33
③ - ④	10	6	2
④ - ⑤	10	6	2
⑤ - ⑥	55	32	9
⑥ - ❶	230	135	38
❶ - ❷	25	15	4
❷ - ⑦	40	24	7
Mean	79	46	13

5.1), it is furthermore worthwhile to estimate the time span of sedimentation recorded by the undisturbed layers sandwiched between the sheet slumps (labeled 1 to 7 in white circles in Fig. 2) and the load casts and plastic intrusions (labeled 1 to 2 in black circles in Fig. 2). The calculated values are given in Table 1 and range for sedimentation rates of 1.7–6 mm/a between 6 and 135 years (mean 46 years) and 2 and 38 years (mean 13 years), respectively. Since the individual sheet slumps were most likely triggered by single earthquake events, the sedimentation times of the undeformed inter-slump deposits could provide estimates for earthquake recurrence intervals. However, since only a few Ms 4–5 earthquakes were recorded since 1900 in the region close to the Hirlatz cave (Hammerl, 2017), a comparison of historic records with our geologically derived estimates of earthquake recurrence intervals would be farfetched.

5.4. Comparison with similar preserved structures

The described soft sediment deformation structures bear many similarities with the folds and faults described from the Late Pleistocene Lisan Formation preserved adjacent to the Dead Sea (Marco et al., 1996; Ken-Tor et al., 2001; Alsop and Marco, 2011, 2012a; 2012b, 2013; 2014; Alsop et al., 2015, 2016; 2017a, 2017b), where varve-like laminated sediments facilitate the recognition of spectacular seismites (Migowski et al., 2004). The deformation features such as asymmetric slump folds, down-slope verging fault-related folds, back-thrusts and refolds typically appear in up to one meter thick layers that are sandwiched between undeformed layers. The structures and their cross-cutting relationships were used to derive the geometry and the progressive evolution of the slumps, involving initiation, translation, cessation, relaxation and compaction phases (Alsop and Marco, 2011). Rather than reiterating all similarities between the investigated structures from the Hirlatz cave and the thoroughly described structures from the Lisan Formation, which are obvious when comparing the pictures in the above cited publications with Figs. 6–8 in the present work, the following discussion focuses on some notable differences:

1) The most obvious difference between the soft-sediment deformation structures in the Lisan Formation and the Hirlatz cave is scale. In the Lisan Formation the slump folds reach wavelengths of several meters and thrusts have displacements of nearly 5 m (Alsop et al., 2017b), whereas the structures in the Hirlatz cave are smaller by two orders of magnitude. The thickness of sheet slumps in multilayers depends on several factors, such as grain size and porosity of the mechanically layered sediments and the size of the detached area. Therefore the thickness of sheet slumps varies significantly in different sedimentary environments (Allen, 1982 and references cited therein): In glacially influenced settings sheet slumps rarely exceed a thickness of 0.5 m, whereas in deltaic, lacustrine and shallow marine sequences their thickness varies between 1 and 10 m. Sheet slumps in deep water basins, which can be laterally traceable for many kilometers, may exceed thicknesses of 100 m. The sheet slumps in the Hirlatz cave do not exceed a thickness of more than a few centimeters and are hence much thinner than most of the slumps described in the literature. Presumably the small size of the detachment area (limited by the dimensions of the cave) led to thin slumps.
2) Structures in sheet slumps from various environmental settings, including the Lisan Formation, are often truncated by an overlying undeformed horizon that caps the slump (Woodcock, 1979; Allen, 1982; Farrell, 1984; Maltman, 1994; Strachan, 2008; Alsop and Marco, 2011, 2012b). Truncation by erosion can be generated in relatively shallow water settings by tsunami and seiche waves that flow back and forth across the slumped surface (Alsop and Marco, 2012b). Alternatively, currents generated during the cessation phase of the slump may travel downslope where they erode and scour the bathymetry created during the same event (Alsop and Marco, 2011), resulting in leveling of topographic highs and infilling of troughs. The frequently observed thinning of horizons above underlying culminations suggests that reworking by secondary currents is sometimes incomplete and a weak bathymetry, which controlled early deposition of the overlying sediments, survived (Alsop and Marco, 2013). The presence of an upper welded contact indicates that deformation was intraformational and related to slumping that occurred at the sediment surface (Alsop and Marco, 2014). Although the Hirlatz cave sheet slumps exhibit similar features and hence must have formed at the sediment surface, erosive truncation of the structures at the upper contact is rarely observed (e.g. Fig. 6e). Note, however, that all recorded slumps must have, at least locally, formed a bathymetry, as revealed by overlying sediments that are thickening/thinning above troughs/culminations. We presume that the rarely observed erosional truncations of the sheet slumps indicate a low-energy depositional environment, a conclusion supported by the varve-like sediments.
3) In the Hirlatz cave sediments, sub-vertical sedimentary injections, sourced from underlying horizons, that cross-cut horizontal beds and layers with soft-sediment deformation structures are absent. In contrast, injections formed by fluidized sediments within the Lisan Formation have confirmed that the folds and thrusts are slump-related and were developing prior to complete lithification of the underlying sequence (Alsop and Marco, 2011). The Hirlatz cave sediments exhibit only diapiric intrusions, which preserve the internal layering of the laminated clay-rich source layer (Fig. 7c and d). Earthquake-induced clastic dikes are natural example of hydraulic fractures combining fracture propagation and laminar or turbulent flow of fluidized sediments (Levi et al., 2011). A coupled fluid-fracture approach suggests that near the surface driving pressures in the order of 1–2 MPa are necessary to generate clastic dikes. Lower pressures may be sufficient to fluidize the source layer, but insufficient for dike injection following hydro-fracturing (Levi et al., 2011). Furthermore, clastic dikes are interpreted to form by earthquakes with magnitudes ranging from 5 to 8 (Audemard and De Santis, 1991; Obermeier, 1996). We therefore conclude that the intensities of the earthquakes causing the soft-sediment deformation structures in the Hirlatz cave were less than c. VI and hence lower than the energy release necessary for generating clastic dikes (Rodríguez-Pascua et al., 2000).

6. Conclusions

1) The investigated varve-like sediments have a glacial origin and were deposited in the Hirlatz cave under phreatic fluvio-lacustrine conditions. The deposition and the syn-sedimentary soft-sediment deformation occurred most likely during the last glaciation (i.e. around 25 ka ago).

2) Nine distinct layers with soft sediment structures exhibit sheets slumps and plastic intrusions that were emplaced following liquefaction and gravitationally induced downslope translation. Structures within the exposed slump toes suggest translation towards the east, which is opposite to the nowadays vadose drainage towards the southwest.
3) The liquefaction and associated formation of soft sediment structures in the fully submerged stratified layers was triggered by episodic seismic events most probably associated with the nearby SEMP strike-slip fault system.
4) The described soft sediment deformation structures bear many similarities with mass transport deposits in slump sheets from the Late Pleistocene Lisan Formation outcropping adjacent to the Dead Sea. However, the structures from the Hirlatz cave are two orders of magnitude smaller, probably due to the small areal size of the detachment horizons constrained by the narrow passage in the cave.
5) To our knowledge, the described structures are the first report of liquefaction and seismically induced soft-sediment deformations in Quaternary sediments in the Eastern Alps.

Acknowledgement

We thank the Austrian Science Foundation FWF (Project SPELEOTECT, P25884-N29) for financial support. Stimulating discussions with Erich Draganits, Klaus Reichert, and Monika Hölzel were greatly beneficial. Harald Bauer, Ina Böhm and Thomas Excel assisted fieldwork in the Hirlatz cave.

Appendix A. Supplementary data

Supplementary data related to this article can be found at http://dx.doi.org/10.1016/j.jsg.2018.02.010.

References

Allen, J.R.L., 1973. A classification of climbing-ripple cross-lamination. J. Geol. Soc. Lond. 129, 537–541.
Allen, J.R.L., 1982. Sedimentary Structures. Their Character and Physical Basis. Elsevier Scientific Publishing Company, Amsterdam 663 pp.
Alsop, G.I., Marco, S., 2011. Soft-sediment deformation within seismogenic slumps of the Dead Sea basin. J. Struct. Geol. 33, 433–457.
Alsop, G.I., Marco, S., 2012a. A large-scale radial pattern of seismogenic slumping towards the Dead Sea Basin. J. Geol. Soc. Lond. 169, 99–110.
Alsop, G.I., Marco, S., 2012b. Tsunami and seiche-triggered deformation within offshore sediments. Sediment. Geol. 261–262, 90–107.
Alsop, G.I., Marco, S., 2013. Seismogenic slump folds formed by gravity-driven tectonics down a negligible subaqueous slope. Tectonophysics 605, 48–69.
Alsop, G.I., Marco, S., 2014. Fold and fabric relationships in temporally and spatially evolving slump systems: a multi-cell flow model. J. Struct. Geol. 63, 27–49.
Alsop, G.I., Weinberger, R., Levi, T., Marco, S., 2015. Deformation within an exposed salt wall: recumbent folding and extrusion of evaporites in the Dead Sea Basin. J. Struct. Geol. 70, 95–118.
Alsop, G.I., Marco, S., Weinberger, R., Levi, T., 2016. Sedimentary and structural controls on seismogenic slumping within mass transport deposits from the Dead Sea Basin. Sediment. Geol. 344, 71–90.
Alsop, G.I., Marco, S., Weinberger, R., Levi, T., 2017a. Upslope-verging back thrusts developed during downslope-directed slumping of mass transport deposits. J. Struct. Geol. 100, 45–61.
Alsop, G.I., Marco, S., Levi, T., Weinberger, R., 2017b. fold and thrust systems in mass transport deposits. J. Struct. Geol. 94, 98–115.
Audemard, F.A., De Santis, F., 1991. Survey of liquefaction structures induced by recent moderate earthquakes. Bull. Int. Assoc. Eng. Geol. 44, 5–16.
Audra, P., Quinif, Y., Rochette, P., 2002. The genesis of the Tennengebirge karst and caves (Salzburg, Austria). J. Caves Karst. Stud. 64, 153–164.
Becker, A., Davenport, C.,A., Eichenberger, U., Gilli, E., Jeannin, P.-Y., Lacave, C., 2006. Speleoseismology: a critical perspective. J. Seismol. 10, 371–388.
Becker, A., Häuselmann, Ph, Gilli, E., 2012. Active tectonics and earthquake destructions in caves of northern and central Switzerland. Int. J. Speleol. 41, 35–49.
Beidinger, A., Decker, K., 2011. 3D geometry and kinematics of the Lassee flower structure: implications for segmentation and seismotectonics of the Vienna Basin strike-slip fault, Austria. Tectonophysics 499, 22–40.
Beidinger, A., Decker, K., Roch, K., 2011. The Lassee segment of the Vienna Basin fault system as a potential source of the earthquake of Carnuntum in the fourth century A.D. Int. J. Earth Sci. 100, 1315–1329.
Brückl, E., Behm, M., Decker, K., Grad, M., Guterch, A., Keller, G.R., Thybo, H., 2010. Crustal structure and active tectonics in the Eastern Alps. Tectonics 29. http://dx.doi.org/10.1029/2009tc002491.
Buchegger, G., Greger, W., 1998. Die Hirlatzhöhle im Dachstein. Die Höhle, Wien 408 pp.
Burollet, P.F., 1975. Tectonique en radeaux en Angola. Bull. Soc. Geol. Fr. S7-XVII, 503–504.
Davis, G.H., Reynolds, S.J., Kluth, C.F., 1996. Structural Geology of Rocks and Regions. John Wiley, Hoboken, pp. 776.
Debacker, T.N., Sintubin, M., Verniers, J., 2001. Large-scale slumping deduced from structural and sedimentary features in the Lower Palaeozoic Anglo-Brabant fold belt, Belgium. J. Geol. Soc. Lond. 158, 341–352.
Debacker, T.N., Dumon, M., Matthys, A., 2009. Interpreting fold and fault geometries from within the lateral to oblique parts of slumps: a case study from the Anglo-Brabant Deformation Belt (Belgium). J. Struct. Geol. 31, 1525–1539.
Decker, K., Peresson, H., Hinsch, R., 2005. Active tectonics and quaternary basin formation along the Vienna basin transform fault. Quat. Sci. Rev. 24, 305–320.
Decker, K., Gangl, G., Kandler, M., 2006. The earthquake of Carnuntum in the fourth century a.d. – archaeological results, seismologic scenario and seismotectonic implications for the Vienna Basin fault, Austria. J. Seismol. 10, 479–495.
Elliott, C.G., Williams, P.F., 1988. Sediment slump structures: a review of diagnostic criteria and application to an example from Newfoundland. J. Struct. Geol. 10, 171–182.
Farrell, S.G., 1984. A dislocation model applied to slump structures, Ainsa Basin, South Central Pyrenees. J. Struct. Geol. 6, 727–736.
Fletcher, R.C., 1982. Analysis of the flow in layered fluids at small, but finite, amplitudes with application to mullion structures. Tectonophysics 81, 51–66.
Ford, D., Williams, P., 2007. Karst Hydrogeology and Geomorphology. Wiley, Chichester, pp. 576.
Franke, H.W., Ilming, H., 1963. Beobachtungen in der Dachstein-Mammuthöhle. Die Höhle 14, 36–40.
Frisch, W., Kuhlemann, J., Dunkl, I., Szekely, B., 2001. The Dachstein paleosurface and the Augenstein Formation in the northern calcareous Alps - a mosaic stone in the geomorphological evolution of the eastern Alps. Int. J. Earth Sci. 90, 500–518.
Frisch, W., Gawlick, H.J., 2003. The nappe structure of the Northern Calcareous Alps and its disintegration during Miocene tectonic extrusion - a contribution to understanding the orogenic evolution of the Eastern Alps. Int. J. Earth Sci. 92, 712–728.
Frost, E., Dolan, J., Sammis, C., Hacker, B., Cole, J., Ratschbacher, L., 2009. Progressive strain localization in a major strike-slip fault exhumed from midseismogenic depths: structural observations from the Salzach-Ennstal- Mariazell-Puchberg fault system, Austria. J. Geophys. Res. 114, 1–14.
Galli, P., 2000. New empirical relationships between magnitude and distance for liquefaction. Tectonophysics 324, 169–187.
Gibert, L., Sanz de Galdeano, C., Alfaro, P., Scott, G., López Garrido, A.C., 2005. Seismic-induced slump in early Pleistocene deltaic deposits of the Baza basin (SE Spain). Sediment. Geol. 179, 279–294.
Grasemann, B., Stüwe, K., Vannay, J.-C., 2003. Sense and non-sense of shear in flanking structures. J. Struct. Geol. 25, 19–34.
Grenerczy, G., Sella, G., Stein, S., Kenyeres, A., 2005. Tectonic implications of the GPS velocity field in the northern Adriatic region. Geophys. Res. Lett. 32. http://dx.doi.org/10.1029/2005GL022947.
Haas, J., Lobitzer, H., Monostori, M., 2007. Characteristics of the Lofer cyclicity in the type locality of the Dachstein limestone (Dachstein plateau, Austria). Facies 53, 113–126.
Hammerl, C., 2017. Historical earthquake research in Austria. Geo sci. Lett. 4, 7. http://dx.doi.org/10.1186/s40562-017-0073-8.
Haneberg, W.C., 1991. Cuspate-lobate folds along a sedimentary contact, Los Lunas volcano, New Mexico. New Mexico Bur. Mines and Mineral Resour. Bull. 137, 162–163.
Heifetz, E., Agnon, A., Marco, S., 2005. Soft sediment deformation by Kelvin Helmholtz instability: a case from Dead Sea earthquakes. Earth Planet. Sci. Lett. 236, 497–504.
Horváth, Z., Michéli, E., Mindszenty, A., Berényi-Üveges, J., 2005. Soft-sediment deformation structures in late Miocene–Pleistocene sediments on the pediment of the Mátra Hills (Visonta, Atkár, Verseg): cryoturbation, load structures or seismites? Tectonophysics 410, 81–95.
Jones, O.T., 1939. The geology of the Colwyn Bay district: a study of submarine slumping during the Salopian period. Quarterly J. Geol. Soc. Lond. 380, 335–382.
Kelling, G., Walton, E., 1957. Load-cast structures: their relationship to upper-surface structures and their mode of formation. Geol. Mag. 94, 481–490.
Ken-Tor, R., Agnon, A., Enzel, Y., Stein, M., Marco, S., Negendank, J.F.W., 2001. High-resolution geological record of historic earthquakes in the Dead Sea basin. J. Geophys. Res. 106, 2221–2234.
Lacave, C., Koller, M.G., Egozcue, J.J., 2004. What can be concluded about seismic history from broken and unbroken speleothems? J. Earthq. Eng. 8, 431–455.
Leroy, Y.M., Triantafyllidis, N., 2001. Stability analysis of incipient folding and faulting of an elasto-plastic layer on a viscous substratum. In: Lehner, F.K., Urai, J.L. (Eds.), Aspects of Tectonic Faulting. Springer, Berlin, Heidelberg.
Levi, T., Weinberger, R., Eyal, Y., 2011. A coupled fluid-fracture approach to propagation of clastic dikes during earthquakes. Tectonophysics 498, 35–44.
Lignier, V., Desmet, M., 2002. Les archives sédimentaires quaternaires de la grotte Sous-les-Sangles (Bas-Bugey, Jura meridional, France). Indices paleo-climatiques et sismotectoniques. Karstologia 39, 27–46.
Linzer, H.-G., Decker, K., Peresson, H., Dell'Mour, R., Frisch, W., 2002. Balancing lateral orogenic float of the Eastern Alps. Tectonophysics 354, 211–237.
Lowe, D.R., 1976. Subaqueous liquefied and fluidized sediment flows and their deposits. Sedimentology 23, 285–308.
Maltman, A., 1994. The Geological Deformation of Sediments. Chapman & Hall, London 362 pp.

Mandl, G.W., 1998. Geologische Karte der Dachsteinregion, 1:50000. Geol. Bundesanstalt, Wien.
Mandl, G.W., 2000. The Alpine sector of the Tethyan shelf; examples of Triassic to Jurassic sedimentation and deformation from the northern calcareous Alps. Mitt. Österr. Geogr. Ges. 92, 61–77.
Marco, S., Stein, M., Agnon, A., 1996. Dead Sea Graben paleoseismology. J. Geophys. Res. 101, 6179–6191.
Martino, S., Prestininzi, A., Romeo, R.W., 2014. Earthquake-induced ground failures in Italy from a reviewed database. Nat. Hazards and Earth Syst. Sci. 14, 799–814.
Michetti, A.M., Esposito, E., Guerrieri, L., Porfido, S., Serva, L., Tatevossian, R., Vittori, E., Audemard, F., Azuma, T., Clague, J., Comerci, V., Gürpinar, A., Mc Calpin, J., Mohammadioun, B., Mörner, N.A., Ota, Y., Roghozin, E., 2007. Environmental Seismic Intensity scale – ESI 2007 La scala di Intensità Sismica basata sugli effetti ambientali – ESI 2007. In: Guerrieri, L., Vittori, E. (Eds.), Memorie descrittive della carta geologica D'Italia LXXIV, Servizio Geologico d'Italia, Dipartimento Difesa del Suolo. APAT, Rome, Italy, pp. 74.
Migowski, C., Agnon, A., Bookman, R., Negendank, J.F.W., Stein, M., 2004. Recurrence pattern of Holocene earthquakes along the Dead Sea transform revealed by varve-counting and radiocarbon dating of lacustrine sediments. Earth Planet. Sci. Lett. 222, 301–314.
Montenat, C., Barrier, P., Ott d'Estevou, P., Hibsch, C., 2007. Seismites: an attempt at critical analysis and classification. Sediment. Geol. 196, 5–30.
Moore, D.M., Reynolds, R.C., 1997. X-ray Diffraction and the Identification and Analysis of clay Minerals. Oxford University Press, pp. 378.
Moretti, M., 2000. Soft-sediment deformation structures interpreted as seismites in middle-late Pleistocene aeolian deposits (Apulian foreland, southern Italy). Sediment. Geol. 135, 167–179.
Obermeier, S.F., 1996. Use of liquefaction-induced features for paleoseismic analysis - an overview of how seismic liquefaction features can be distinguished from other features and how their regional distribution and properties of source sediment can be used to infer the location and strength of Holocene paleo-earthquakes. Eng. Geol. 44, 1–76.
Owen, G., 1987. Deformation processes in unconsolidated sands. Geol. Soc. Lond. Spec. Publ. 29, 11–24.
Passchier, C.W., 2001. Flanking structures. J. Struct. Geol. 23, 951–962.
Plan, L., Grasemann, B., Spötl, C., Decker, K., Boch, R., Kramers, J., 2010. Neotectonic extrusion of the Eastern Alps: constraints from U/Th dating of tectonically damaged speleothems. Geology 38, 483–486.
Pohl, H., Greger, W., 2001. Die längste Höhle Österreichs - Die Hirlatzhöhle bei Hallstatt/Dachstein/Salzkammergut. 3. Symposioum zur Geschichter der Erdwissenschaften in Österreich. pp. 83–84.
Postpischl, D., Agostini, S., Forti, P., Quinif, Y., 1991. Palaeoseismicity from karst sediments: the "Grotta del Cervo" cave case study (Central Italy). Tectonophysics 193, 33–44.
Ramsay, J.G., Huber, I.M., 1987. The Techniques of modern structural geology. Folds and Fractures, vol. 2. Academic Press Inc. Ltd, London, pp. 309–700.
Reinecker, J., Lenhardt, W.A., 1999. Present-day stress field and deformation in eastern Austria. Int. J. Earth Sci. 88, 532–550.
Robl, J., Hergarten, S., Stüwe, K., 2008. Morphological analysis of the drainage system in the Eastern Alps. Tectonophysics 460, 263–277.
Rodríguez-Pascua, M.A., Calvo, J.P., De Vicente, G., Gómez-Gras, D., 2000. Soft-sediment deformation structures interpreted as seismites in lacustrine sediments of the Prebetic Zone, SE Spain, and their potential use as indicators of earthquake magnitudes during the Late Miocene. Sediment. Geol. 135, 117–135.
Schauberger, O., 1957. Die Hirlatzhöhle bei Hallstatt (Oberösterreich). Die Höhle 8, 65–67.
Schmid, S.M., Fügenschuh, B., Kissling, E., Schuster, R., 2004. Tectonic map and overall architecture of the Alpine orogen. Eclogae Geol. Helv. 97, 93–117.
Schröckenfuchs, T., Bauer, H., Grasemann, B., Decker, K., 2015. Rock pulverization and localization of a strike-slip fault zone in dolomite rocks (Salzach–Ennstal–Mariazell–Puchberg fault, Austria). J. Struct. Geol. 78, 67–85.
Seemann, R., 1973. Die Genese der Pyrite der Karstgebiete der Nördlichen Kalkalpen. unpulbished PhD Thesis. University of Vienna.
Seilacher, A., 1969. Fault-graded beds interpreted as Seismites. Sedimentology 13, 155–159.
Serpelloni, E., Vannucci, G., Anderlini, L., Bennett, R.A., 2016. Kinematics, seismotectonics and seismic potential of the eastern sector of the European Alps from GPS and seismic deformation data. Tectonophysics 688, 157–181.
Simony, F., 1847. Zweiter Winteraufenthalt auf dem Hallstätter Schneegebirge und drei Ersteigungen der hohen Dachsteinspitze (am 29. Jänner, 4. und 6. February 1847). In: Haidinger, W. (Ed.), Berichte über die Mittheilungen von Freunden der Naturwissenschaft in Wien. vol. 2. pp. 207–221.
Sorby, H.C., 1859. On the structure produced by the currents during the deposition of stratified rocks. Geol. 2, 137–147.
Spengler, E., 1928. Über die Länge und Schubweite der Decken in den nördlichen Kalkalpen. Geol. Rundsch. 19, 1–26.
Spöcker, R.G., 1925. Die Mammuthöhle im Dachstein. Mitt. Höhlen- u. Karstforsch. pp. 70–79.
Strachan, L.J., 2002. Slump-initiated and controlled syndepositional sandstone remobilization: an example from the Namurian of County Clare, Ireland. Sedimentology 49, 25–41.
Strachan, L.J., Alsop, G.I., 2006. Slump folds as estimators of palaeoslope: a case study from the Fisherstreet Slump of County Clare, Ireland. Basin Res. 18, 451–470.
Strachan, L.J., 2008. Flow transformations in slumps: a case study from the Waitemata Basin, New Zealand. Sedimentology 55, 1311–1332.
Tesauro, M., Hollenstein, C., Egli, R., Geiger, A., Kahle, H.-G., 2006. Analysis of central western Europe deformation using GPS and seismic data. J. Geodyn. 42, 194–209.
Tollmann, A., 1976. Der Bau der Nördlichen Kalkalpen: orogene Stellung und regionale Tektonik. Deuticke, Wien 449 pp.
Tuttle, M.P., 2001. The use of liquefaction features in paleoseismology: lessons learned in the New Madrid seismic zone, central United States. J. Seismol. 5, 361–380.
Vandenberghe, J., 1988. Cryoturbations. In: Clark, M.J. (Ed.), Advances in Periglacial Geomorphology. John Wiley and Sons, New York, pp. 179–198.
Völkl, G., 1998. Die Hirlatzhöhle als Fenster zu den karsthydrologischen Vorgängen im Inneren des Dachsteins. In: In: Buchegger, G., Greger, W. (Eds.), Die Hirlatzhöhle im Dachstein. Die Höhle suppl. 52. pp. 208–213.
Waldron, J.W.F., Gagnon, J.-F., 2011. Recognizing soft-sediment structures in deformed rocks of orogens. J. Struct. Geol. 33, 271–279.
Wetzler, N., Marco, S., Heifetz, E., 2010. Quantitative analysis of seismogenic shear-induced turbulence in lake sediments. Geology 38, 303–306.
Wiesmayr, G., Grasemann, B., 2005. Sense and non-sense of shear in flanking structures with layer-parallel shortening: implications for fault-related folds. J. Struct. Geol. 27, 249–264.
Williams, B.J., Prentics, J.E., 1957. Slump structures in the Ludlovian rocks of north Herefordshire. Proc. Geol. Assoc. 68, 286–293.
Woodcock, N.H., 1979. The use of slump structures as palaeoslope orientation estimators. Sedimentology 26, 83–99.